lubricants

MDPI

Article

Significance of Thermophoretic Particle Deposition, Arrhenius Activation Energy and Chemical Reaction on the Dynamics of Wall Jet Nanofluid Flow Subject to Lorentz Forces

Umair Khan [1,2], Aurang Zaib [3], Anuar Ishak [1], Iskandar Waini [4], Zehba Raizah [5], Nattakan Boonsatit [6,*], Anuwat Jirawattanapanit [7] and Ahmed M. Galal [8,9]

[1] Department of Mathematical Sciences, Faculty of Science and Technology, Universiti Kebangsaan Malaysia (UKM), Bangi 43600, Malaysia
[2] Department of Mathematics and Social Sciences, Sukkur IBA University, Sukkur 65200, Pakistan
[3] Department of Mathematical Sciences, Federal Urdu University of Arts, Science & Technology, Karachi 75300, Pakistan
[4] Fakulti Teknologi Kejuruteraan Mekanikaldan Pembuatan, Universiti Teknikal Malaysia Melaka, Hang Tuah Jaya, Melaka 76100, Malaysia
[5] Department of Mathematics, College of Science, King Khalid University, Abha 61421, Saudi Arabia
[6] Department of Mathematics, Faculty of Science and Technology, Rajamangala University of Technology Suvarnabhumi, Nonthaburi 11000, Thailand
[7] Department of Mathematics, Faculty of Science, Phuket Rajabhat University (PKRU), Phuket 83000, Thailand
[8] Department of Mechanical Engineering, College of Engineering in Wadi Alddawasir, Prince Sattam Bin Abdulaziz University, AlKharj 11942, Saudi Arabia
[9] Production Engineering and Mechanical Design Department, Faculty of Engineering, Mansoura University, P.O. Box 35516, Mansoura 35516, Egypt
* Correspondence: nattakan.b@rmutsb.ac.th

Citation: Khan, U.; Zaib, A.; Ishak, A.; Waini, I.; Raizah, Z.; Boonsatit, N.; Jirawattanapanit, A.; Galal, A.M. Significance of Thermophoretic Particle Deposition, Arrhenius Activation Energy and Chemical Reaction on the Dynamics of Wall Jet Nanofluid Flow Subject to Lorentz Forces. *Lubricants* **2022**, *10*, 228. https://doi.org/10.3390/lubricants10100228

Received: 23 August 2022
Accepted: 16 September 2022
Published: 20 September 2022

Abstract: The need for effective heating and cooling systems in the automotive, chemical, and aerospace industries is driving a rapid proliferation of heat-transfer technology. In recent times, GO (Graphene Oxide) has been emerging as one of the most promising nanoparticles because of its uninterrupted behavior of electrical conductivity even at a minimum carrier concentration. Due to this incentive, the behavior of jet flow with heat and mass transfer features of electrically conducting based kerosene oil (KO) fluid dispensed by graphene nanoparticles was studied. In addition, the activation energy, irregular heat source/sink, thermophoretic particle deposition, and chemical reaction are also provoked. In order to provide numerical results, the boundary value problem of fourth-order (bvp4c) solver was used. The graphs were used to illustrate the effects of relevant parameters on the fluid flow, heat, and mass transfer rates. The incorporation of graphene nanoparticles significantly improves heat conductivity. Additionally, the nanoparticle volume fraction augments the temperature and concentration profile while the velocity profile declines. Moreover, the temperature enhances due to the heat source, whilst the contrary behavior is observed in the presence of the heat sink. Furthermore, the shear stress increases up to 12.3%, the Nusselt number increases up to 0.119%, and the Sherwood number increases up to 0.006% due to the presence of nanofluid. Finally, we can conclude that the latest work will be useful for thermal cooling systems, including cooling for engines and generators, nuclear systems, aviation refrigeration systems, and other systems.

Keywords: jet flow; nanofluid; activation energy; heat source/sink; thermophoretic particle deposition

1. Introduction

The past century has witnessed a revolution in the industries by employing extraordinary applications of nanofluids including electrical cooling, power generation, solar energy, building technology, and plant processing. Nanofluid offers novel alternate substances to

utilize in several fields [1,2], one of them is the improvement of lubricants [3,4]. Graphene Oxide (GO) is among the most promising nanoparticles given its constant electrical conductivity even at low carrier concentrations. GO has an extremely high electron mobility when compared to other available particles. External magnetic fields have the power to control the heat-transfer and flow properties as well as the thermal and physical properties of magnetic nanofluids. This is highly beneficial for managing processes in metallurgy. A simple method used to create a nanocomposite of Co_3O_4 nanoparticles embedded in conducting graphene as an improved anode material for battery cells was disclosed by Wu et al. [5]. They discovered that the Co_3O_4/graphene nanocomposite exhibits superior rechargeable performance with a significant amount of reversible capacity. Graphene-based particles have garnered a great deal of interest for usage in energy storage. Pumera [6] outlined the experimental as well as a theoretical exploration of using graphene-based applications such as storage systems of hydrogen, and lithium batteries. Ahmad et al. [7] present one of the significant uses of graphene in relation to electrical conductivity. Khan et al. [8] explored the magnetic impact on the nanofluid flow through the stretchable cylinder and found that the magnetic and thin film parameters decelerate the velocity and accelerate the temperature distribution. The non-Newtonian (Casson and Williamson) non-steady flow and thermal properties of electrically conducting water-based thin fluid film dispensed with graphene nanoparticles via a stretchy surface were considered by Ahmad et al. [9]. They observed that the low resistance for heat conduction is provided by the greater surface area of the film thickness due to graphene nanoparticles. Recently, Khan et al. [10] investigated the buoyancy flow of water-based graphene nanoparticles through a vertical surface with radiation impact and performed a stability analysis to find a stable solution.

Thermophoresis particle deposition in a fluid flow is important in several technical processes, including the protection of nuclear reactors, air cleaners, heat exchangers, and burners for powdered coal. The thermophoresis phenomenon is caused by several categories of particles acting differently when exposed to a temperature difference. Tiny particles dispersed in an NIG (non-isothermal gas). will reach a velocity during thermophoresis. This process greatly increases the deposition velocity of tiny particles in the direction of cooling temperature, while it has no effect on large particles. Thermophoresis allows small particles to mend on a cold surface. Alam et al. [11] inspected 2D (two-dimensional) steady magneto flow across an inclined semi-infinite plate including thermophoresis and erratic suction. They found that the suction parameter uplifts the thermal and concentration boundary layer thicknesses. The mixed convection flow through a vertical sheet with a magnetic effect and thermophoresis effect was examined by Damseh et al. [12]. They observed that the velocity of fluid decreases due to magnetic numbers. Rahman [13] demonstrated the thermophoretic particle deposition and enforced magnetic influence on the flow of nanofluid through the rotating system. It has been found that the rate at which thermophoretic particles deposit is greatly influenced by thermal diffusion, slip mechanism, magnetic field, diffusion-thermo, and radiation. Recently, numerous authors [14–18] have also reported the impact of thermophoretic particle deposition under diverse circumstances.

Numerous chemicals, mechanical, and manufacturing processes depend heavily on chemical changes. A large amount of oxygen known as activation energy is needed to control a process. The energy needed to initiate a chemical reaction is often referred to as activation energy. The fundamental idea behind this topic was created in 1889 by Svante Arrhenius. Shafique et al. [19] observed that the chemical reaction in connection to activation energy has a significant impact on the fluid-flow behavior. They discovered that the solute content in a binary mixture correlates with the activation energy and the rotation parameter. Khan et al. [20] explored the impact of activation energy on the radiative 3D (three-dimensional) flow induced by a cross nanofluid with binary chemical reaction by employing the Buongiorno model. It can be seen from the generated graphical data that Brownian motion and thermophoresis have a major impact on the heat-transfer process. The effects of Joule heating and activation energy with binary chemical change incorporating the MHD (magneto-hydrodynamics) Jeffrey fluid towards a contoured compressed

surface were reviewed by Khan and Alzahrani [21]. They revealed that the curvature parameter enhances the entropy generation. Najafabadi et al. [22] studied the effects of radiation, conduction, and convection heat transfer in a movable fin with even velocity and changeable thermal conductivity. Rana et al. [23] utilized the non-Newtonian model to investigate the blood flow incorporated nanofluid through bio-convection with activation energy and chemical reaction. Recently, Reza-E-Rabbi et al. [24] investigated the radiative magnetism flow of a Casson nanofluid past a stretchy periphery with activation energy and chemical reaction. They observed that the temperature is elevated due to Brownian motion, thermophoretic, and radiation effects.

The migration of gaseous particles from hot to cold locations is known as thermophoresis. This process informs the system that micron-sized particles are prohibited in non-isothermal gas and move more quickly along the path of reducing thermal gradients. The significance of theoretical and experimental understanding of thermophoretic particle deposition cannot be understated due to its wide range of thermal engineering and industrial applications. The distribution of temperature and the deposition of particles may change as a result of thermogenesis' possible effects. These include heat exchangers, air cleaners, filtration, powdered coal burners, environmental and atmospheric pollution, ventilation systems in buildings, and safety for nuclear reactors. Previous explorations on the thermophoresis problem were presented by Goren [25], Talbot et al. [26], Mills et al. [27], and Batchelor and Shen [28]. Tsai [29] provided a straightforward method to examine the thermophoresis impact on the flow past a flat surface, which was inspired by earlier investigations. In this study, the thermophoresis is calculated by using a first-order chemical reaction and suction-like convection term. The hydromagnetic flow was then studied by Chamkha and Issa [30], and the porous medium impact was considered by Chamkha and Pop [31]. Alam et al. [32] additionally investigated the flow on an adiabatic porous sheet. Their studies revealed that the Nusselt number for the injection of fluid is sensitive due to the increasing inclination of the angle. Moreover, the changeable properties of the fluid were presented by Das et al. [33]. Notably, the fluid flow through a shrinkable sheet incorporating thermophoresis was observed by Sinha and Misra [34] and Zaib and Shafie [35]. In recent times, Jyothi et al. [36] explored the flow flanked by parallel plates with thermophoresis whereas Shah et al. [37] examined the flow of a second-grade fluid across a flat plate induced by erratic fluid properties.

The temperature of the entering jet should vary from that of the static fluid in industrial applications of jets such as melting plastic and metal sheets, drying fabrics, chilling microelectronic equipment, etc. As a result, the thermal boundary equation needs to be solved. It appears that Tetervin [38] presented the first solution for the conventional laminar wall jet. A famous non-trivial exact solution with exponential decline at infinity (e-jet) was obtained by Glauert [39]. Riley [40] investigated the thermal features of the preheated radial jet. Schwarz and Caswell [41] analyzed the characteristics of heat transfer in connecting to the Glauert wall jet flow, in which they presented the closed form solution including the impact of steady heat-flux and temperature. An approximate solution to the time-dependent energy equation was provided by Gorla [42] in the context of Glauert's wall jet flow. It has been shown that the features of heat transfer can be reduced when a variation in surface temperature is imposed. Aly and Pop [43] inspected the hybrid nanofluid induced by wall jet flow with thermal energy and found dual solutions. It was discovered that only suction makes the lower-branch and the upper-branch solutions conceivable.

The literature indicates that no effort has been made to investigate jet flow induced by oil-based graphene nanofluid including thermophoretic particle deposition, activation energy with chemical reaction, and erratic heat sink/source. Therefore, the novelty of the present work is to inspect the jet flow of GO nanofluid by including the thermophoretic particle deposition, activation energy with chemical reaction, and erratic heat source/sink which will close this research gap. The leading flow equations are turned into a set of ODEs (ordinary differential equations). The well-known bvp4c is used to solve the resulting equations. The objective is to improve the regular fluid's thermal conductivity for a better

heat-transport phenomenon through portable density and heat exchangers employed in contemporary thermal procedures. The effects of all relevant parameters on the velocity, concentration, and temperature were graphically displayed and explained.

2. Mathematical Background of the Problem

Consider the phenomenon of the Glauert model which is schematically highlighted in the form of Figure 1. In this model, a 2D MHD laminar wall jet heat and mass transfer flow of nanofluid blown from a thin slit on the upper section of a static permeable surface with influences of an irregular heat sink/source was explored. Further, the analysis of the given problem also comprised the significant effect of thermophoretic particle deposition and Arrhenius activation energy with chemical reaction. It is assumed that the coordinates of the x- and y- axes are measured along the wall and orthogonal to it, respectively. The uniform wall temperature and ambient temperature are denoted by T_w and T_∞, respectively. Further, assume that $C = C_w = 0$ and C_∞ represent the respective uniform wall and ambient concentration of the fluid. However, the irregular heat sink/source term is taken in the posited energy equation which is symbolically denoted by Q''' and later it is explained in detail. Additionally, the magnetic field [44,45] is taken as $B = B_0 x^{-3/4}$ to obtain the similarity equations. Meanwhile, B_0 denotes the magnetic field strength. These suppositions allow the leading equations to be formulated as [42,43]:

$$\frac{\partial u}{\partial x} + \frac{\partial v}{\partial y} = 0, \tag{1}$$

$$u\frac{\partial u}{\partial x} + v\frac{\partial u}{\partial y} = \frac{\mu_{nf}}{\rho_{nf}}\frac{\partial^2 u}{\partial y^2} - \frac{\sigma_{nf}}{\rho_{nf}}B^2 u, \tag{2}$$

$$(\rho c_p)_{nf}\left(u\frac{\partial T}{\partial x} + v\frac{\partial T}{\partial y}\right) = k_{nf}\frac{\partial^2 T}{\partial y^2} + Q''' \tag{3}$$

$$u\frac{\partial C}{\partial x} + v\frac{\partial C}{\partial y} = D_f\frac{\partial^2 C}{\partial y^2} - \frac{\partial}{\partial y}(V_{TPD}C) - k_r^2(x)\left(\frac{T}{T_\infty}\right)^m e^{\frac{-E_0}{k_f T}}(C - C_\infty), \tag{4}$$

subject to the BCs (boundary conditions) are:

$$\left.\begin{array}{c} u = 0,\ v = v_w(x) = -\sqrt{v_f}x^{-3/4}f_{wa},\ T = T_w,\ C = C_w = 0 \ \text{ at } y = 0, \\ u \to 0,\ T \to T_\infty,\ C \to C_\infty \text{ as } y \to \infty. \end{array}\right\} \tag{5}$$

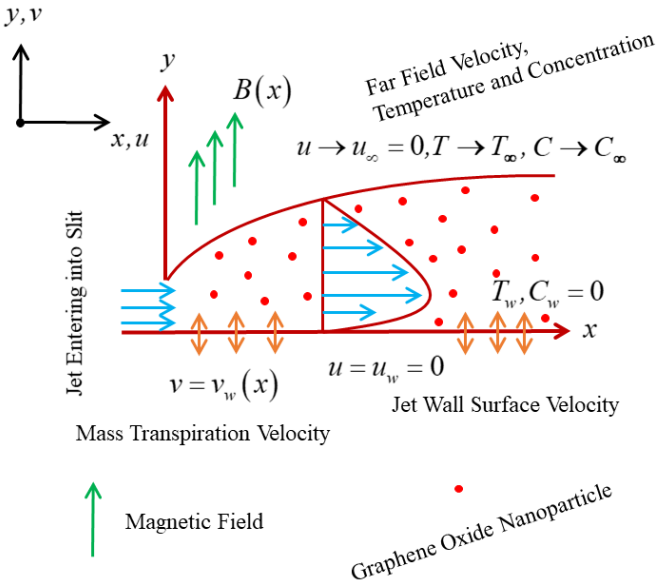

Figure 1. Physical configuration of the wall jet flow embedded nanofluid.

Here, u and v are the components of velocity along the respective x- and y- axes while T and C are the temperature and concentration of the nanofluid. It is further assumed that the mass transpiration velocity is $v_w(x) = -\sqrt{\alpha_f}x^{-3/4}f_{wa}$ where v_f signifies the respective kinematic viscosity and f_{wa} the mass injection/suction parameter. Furthermore, D_f identifies the mass diffusion coefficient, E_a the activation energy, and $k_r^2(x)$ the variable chemical reaction rate which is delineated later mathematically. Additionally, the final term Q''' on the RHS (right hand side) of Equation (4) demonstrates the role of the erratic heat source/sink, which can be illustrated as [see [46]]:

$$Q''' = \frac{k_{nf}u_r(x)}{xv_{nf}}\left[A_a^*(T_w - T_\infty)e^{-\xi} + B_a^*(T - T_\infty)\right], \tag{6}$$

where $u_r(x) = 4x^{-1/2}$ is the reference velocity which is occupied by Raees et al. [47] and the temperature-dependent heat sink/source and the exponentially decaying space coefficients are distinguished by B_a^* and A_a^*, respectively. Consequently, the positive values of A_a^* and B_a^* correspond to the phenomenon of a heat generation source factor while the negative values of A_a^* and B_a^* correspond to the phenomenon of the heat generation sink factor.

In the aforementioned stated equations, the mathematical representations exercised for the nanofluid (NF) are heat capacity $(\rho c_p)_{nf}$, thermal conductivity k_{nf}, electrical conductivity σ_{nf}, dynamic viscosity μ_{nf}, and the requisite posited density ρ_{nf}. The NF model expressions or correlations thermo-physically can be written as follows:

$$\frac{\mu_{nf}}{\mu_f} = \frac{1}{(1-\varphi)^{2.5}}, \frac{\rho_{nf}}{\rho_f} = \varphi\left(\frac{\rho_{snp}}{\rho_f}\right) + (1-\varphi), \tag{7}$$

$$\frac{\sigma_{nf}}{\sigma_f} = \frac{\sigma_{snp} + 2\sigma_f - 2\left(\sigma_f\varphi - \sigma_{snp}\varphi\right)}{\sigma_{snp} + 2\sigma_f + 1\left(\sigma_f\varphi - \sigma_{snp}\varphi\right)}, \tag{8}$$

$$\frac{k_{nf}}{k_f} = \frac{k_{snp} + 2k_f - 2\varphi\left(k_f - k_{snp}\right)}{k_{snp} + 2k_f + \varphi\left(k_f - k_{snp}\right)}, \tag{9}$$

$$\frac{(\rho c_p)_{nf}}{(\rho c_p)_f} = \varphi\left(\frac{(\rho c_p)_{snp}}{(\rho c_p)_f}\right) + (1-\varphi). \tag{10}$$

Hence, the aforementioned leading equations exemplify the thermo-physical properties of the kerosene-oil-based graphene oxide nanofluid, where φ indicates the volume fraction of the nanoparticles. Additionally, the subscripts snp and f are the nanoparticles and the base working fluid (KO). Here, the shape factor is taken as a sphere whose value is 3. Generally, the data of the graphene oxide (GO) nanoparticles along with the regular-based fluid (KO) are provided in Table 1.

Table 1. Experimental physical data of the base fluid and GO nanoparticles [9,10,48].

Properties	ρ(kg/m^3)	c_p(J kgK)	k (W/mk)	σ(S/m)	Pr
Kerosene Oil	783	2090	0.145	21×10^{-6}	23.004
GO	1800	717	5000	6.3×10^{7}	—

2.1. Similarity Variables

To ease the examination of the considered wall jet flow phenomenon, we stated the subsequent self-similarity variables according to Glauert [39] which are as follows:

$$\xi = \left(v_f^2x^3\right)^{-1/4}y, \psi = \left(v_f^2x\right)^{1/4}F(\xi), G(\xi) = \frac{T - T_\infty}{T_w - T_\infty}, S(\xi) = \frac{C - C_\infty}{C_w - C_\infty} \tag{11}$$

where ψ is the stream function and signified as $u = \partial\psi/\partial y$ and $v = -\partial\psi/\partial x$. Thus, the velocity component is calculated more simply in the form as follows:

$$u = 4x^{-1/2}F'(\xi), \;\; v = -x^{-3/4}\sqrt{v_f}\big(F(\xi) - 3\xi F'(\xi)\big) \tag{12}$$

2.2. Momentum Similarity Equation

For the momentum similarity equations, it is necessary to exercise the similarity variables of Equation (11) early along with the derived velocity components of Equation (12) into the governing Equations (1) and (2) which holds the continuity equation directly while the momentum equation is reduced to the form as:

$$\frac{\mu_{nf}/\mu_f}{\rho_{nf}/\rho_f}F''' + FF'' + 2F\prime^2 - \frac{\sigma_{nf}/\sigma_f}{\rho_{nf}/\rho_f}M_aF' = 0 \tag{13}$$

where $M_a = \frac{\sigma_f B_0^2}{\rho_f}$ is called the magnetic parameter.

2.3. Energy Similarity Equation

It is better to write the state of Equation (3) in a more simplified form, therefore, we incorporate the expression of the non-uniform heat source/sink Q''' term to obtain the form as:

$$u\frac{\partial T}{\partial x} + v\frac{\partial T}{\partial y} = \frac{k_{nf}}{(\rho c_p)_{nf}}\frac{\partial^2 T}{\partial y^2} + \frac{k_{nf}u_r(x)\rho_{nf}}{x\mu_{nf}(\rho c_p)_{nf}}\Big[A_a^*(T_w - T_\infty)e^{-\xi} + B_a^*(T - T_\infty)\Big] \tag{14}$$

In addition, substituting the respective similarity transformations (11) into the Equation (14) reduces to the following requisite posited dimensionless form as follows:

$$\frac{k_{nf}}{k_f}G'' + \mathrm{Pr}\frac{(\rho c_p)_{nf}}{(\rho c_p)_f}FG' + 4\frac{\left(k_{nf}/k_f\right)\left(\rho_{nf}/\rho_f\right)}{\mu_{nf}/\mu_f}\left(A_a^*e^{-\xi} + B_a^*G\right) = 0, \tag{15}$$

where $\mathrm{Pr} = \frac{v_f}{\alpha_f}$ is called the Prandtl number.

2.4. Concentration Similarity Equation

Before moving towards the working procedure of the concentration similarity equation, it is helpful to first define the logical term in Equation (4). The second-last term on the RHS of Equation (4) represents the thermophoretic particle deposition which is symbolically denoted by V_{TPD} and mathematically expressed as:

$$V_{TPD} = -\frac{k_a v_f}{T_a}\frac{\partial T}{\partial y} \tag{16}$$

where T_a is a reference temperature and k_a is the thermophoretic coefficient with a range of values from 0.2 to 1.2 as designated by Batchelor and Shen [28]. Moreover, to obtain a similarity solution of the concentration equation after the use of variables, here, we express the variable reaction rate as $k_r^2(x) = k_0^2x^{-3/2}$. Additionally, by plugging this equation and Equation (16) along with the self-similarity Equation (11) into the acquired leading governing Equation (4). Hence, one obtains the form as:

$$\frac{1}{Sc_a}S'' + FS' - \beta_a(1 + \delta_a G)^m \exp\left(\frac{-E_a}{1 + \delta_a G}\right)S + \Sigma_a\big(G''S + S'G'\big) = 0, \tag{17}$$

where $Sc_a = \frac{v_f}{D_f}$,$\beta_a = k_0^2$, $\delta_a = \frac{T_w - T_\infty}{T_\infty}$,$E_a = \frac{E_0}{k_f T_\infty}$, and $\Sigma_a = \frac{k_a(T_w - T_\infty)}{T_a}$ are called the Schmidt number, the chemical reaction rate, the temperature difference parameter, the activation energy parameter, and the thermophoretic parameter, respectively.

2.5. Transformed Boundary Conditions

According to the use of similarity Equation (11) in Equation (5), we obtain

$$\begin{cases} F(0) = f_{wa},\ F'(0) = 0,\ G(0) = 1,\ S(0) = 0 \text{ at } \xi = 0, \\ F'(\xi) \to 0,\ G(\xi) \to 0,\ S(\xi) \to 1 \text{ as } \xi \to \infty. \end{cases} \tag{18}$$

Here, f_{wa} signifies the constant mass suction/injection factor with ($f_{wa} > 0$) for the mass suction and ($f_{wa} < 0$) for the mass injection.

2.6. Gradients

In the present study, the following key gradients (the skin friction coefficient $\left(C_f\right)$, the Nusselt number (Nu_x), and the Sherwood number (Sh_x)) are expressed as:

$$C_f = \frac{1}{\rho_f u_r^2}\left(\mu_{nf}\frac{\partial u}{\partial y}\bigg|_{y=0}\right), Nu_x = \frac{x}{k_f(T_w - T_\infty)}\left(-k_{nf}\frac{\partial T}{\partial y}\bigg|_{y=0}\right), Sh_x = \frac{x}{D_f C_\infty}\left(D_f\frac{\partial C}{\partial y}\right)\bigg|_{y=0} \tag{19}$$

where k_{nf} and μ_{nf} are the corresponding thermal conductivity and viscosity of the nanofluid. Now, employing the self-similarity transformations in the above stated Equation (19), we obtain

$$2\sqrt{\mathrm{Re}_x}C_f = \frac{\mu_{nf}}{\mu_f}F''(0), \frac{2Nu_x}{\sqrt{\mathrm{Re}_x}} = -\frac{k_{nf}}{k_f}G'(0), \frac{2Sh_x}{\sqrt{\mathrm{Re}_x}} = S'(0). \tag{20}$$

where $\mathrm{Re}_x = \frac{u_r x}{v_f}$ is called the local Reynolds number.

3. Numerical Methodology

This portion of the examination describes the complete working procedure (WP) as well as the reliability, confirmation, or validation of the given scheme. Initially for the WP, it is better to exercise the set or structure of the acquired bounded ordinary differential Equations (13), (15) and (17), along with the boundary restrictions (18). These equations were computationally simulated using the bvp4c solver, which relies on the 3-stage Lobatto IIIA algorithm or formula. In addition, there are several techniques such as RKF-45 (Runge-Kutta-Fehlberg fourth fifth order shooting method), shooting, and Keller box. However, the bvp4c is simple to use and has better accuracy. In the bvp4c technique, the structure of higher-order ODEs is altered into first-order ODEs to apply this technique. Let the variables be:

$$F = \Sigma_1, F' = \Sigma_2, F'\prime = \Sigma_3, G = \Sigma_4, G' = \Sigma_5, S = \Sigma_6, S' = \Sigma_7, \tag{21}$$

$$\frac{d}{d\xi}\begin{pmatrix}\Sigma_1\\ \Sigma_2\\ \Sigma_3\\ \Sigma_4\\ \Sigma_5\\ \Sigma_6\\ \Sigma_7\end{pmatrix} = \begin{pmatrix} \Sigma_2 \\ \Sigma_3 \\ \frac{\rho_{nf}/\rho_f}{\mu_{nf}/\mu_f}\left(-\Sigma_1\Sigma_3 - 2\Sigma_2^2 + \frac{\sigma_{nf}/\sigma_f}{\rho_{nf}/\rho_f}M_a\Sigma_2\right) \\ \Sigma_5 \\ \frac{1}{k_{nf}/k_f}\left(-\mathrm{Pr}\frac{(\rho c_p)_{nf}}{(\rho c_p)_f}\Sigma_1\Sigma_5 - 4\frac{(k_{nf}/k_f)(\rho_{nf}/\rho_f)}{(\mu_{nf}/\mu_f)}\left(A_a^* e^{-\xi} + B_a^*\Sigma_4\right)\right) \\ \Sigma_7 \\ Sc_a\left(-\Sigma_1\Sigma_7 + \beta_a(1+\delta_a\Sigma_4)^m \exp\left(\frac{-E_a}{(1+\delta_a\Sigma_4)}\right)\Sigma_6 - \Sigma_a\Sigma_5\Sigma_7 - \Sigma_a\Sigma_6\frac{d\Sigma_5}{d\xi}\right) \end{pmatrix} \tag{22}$$

and the changed initial conditions are

$$\begin{pmatrix} \Sigma_1(0) \\ \Sigma_2(0) \\ \Sigma_2(\infty) \\ \Sigma_4(0) \\ \Sigma_4(\infty) \\ \Sigma_6(0) \\ \Sigma_6(\infty) \end{pmatrix} = \begin{pmatrix} f_{wa} \\ 0 \\ 0 \\ 1 \\ 0 \\ 0 \\ 1 \end{pmatrix}. \tag{23}$$

In the present study, tolerance $\varepsilon = 10^{-6}$ is applied throughout the computation to meet the convergence criterion. Further, the proposed simulation technique needs initial or preliminary estimates to satisfy the boundary condition (23). In other geometry problems, the initial assumption for the first solution is fairly straightforward, but in the case of the wall jet nanofluid flow problem, it is a little more challenging. As a response, it is preferable to select the values of the other constant parameters that are pertinent to obtaining the necessary results quickly or easily. The computation range of numerical integration is $\xi_{\max} = 25$, which is sufficient for the graphical results to meet the requirement of boundary asymptotically.

Numerical Authentication of the Scheme

This aspect of the work illustrates the crucial aspect of the acknowledged accuracy, dependability, authenticity, or validation of the regarded numerical code. Therefore, it is preferable to create a graph or build a numerical table so that we can compare the new work with the published work for some limiting cases to verify the given code. Here, in this study, a possible Table 2 was prepared for the numerical values of shear stress with varying φ when $f_w = 0$, and $M_a = 0$. From the numerical table, it can be shown that the single current output of shear stress matched with the previously published works of Glauert [39] and Waini et al. [49] extremely accurately. Henceforth, the recent and earlier research are very well matched, therefore, we are confident that the wall jet flow problem will be solved using the suggested technique.

Table 2. Numerical comparison values of shear stress $\frac{\mu_{nf}}{\mu_f} F''(0)$ for several values of φ when $f_w = 0$, and $M_a = 0$.

φ	Glauert [39]	Waini et al. [49]	Present
0.000	$2/9 \approx 0.2222$	0.2222	0.2222
0.035	-	-	0.3178
0.037	-	-	0.3656
0.039	-	-	0.4132

4. Analysis of the Results

This section breakdown was focused on interpreting the whole set of data for the dynamics of the wall jet heat and mass transfer characteristics flow of the kerosene-oil-based graphene oxide nanoparticles due to the influence of many unique parameters. The given problem comprised different control influential parameters such as the solid nanoparticle volume fraction φ, the magnetic parameter M_a, the thermophoretic parameter Σ_a, the radiation parameter R_d, the activation parameter E_a, the chemical reaction rate parameter β_a, the dimensionless temperature difference parameter δ_a, and the mass transpiration parameter f_{wa}. The effects of these parameters on the velocity profile $F'(\xi)$, temperature profile $G(\xi)$, concentration profile $S(\xi)$, shear stress $\left(\mu_{nf}/\mu_f\right)F''(0)$, heat-transfer rate $-\left(k_{nf}/k_f + (4/3)R_d\right)G'(0)$, and mass transfer rate $S'(0)$, are shown in Figures 2–14 as well as in Tables 3–5. For numeric calculations, the fixed values of the distinguished constraints were the following: $\varphi = 0.025$, $m = 1$, $M_a = 0.05$, $\Sigma_a = 0.5$, $f_{wa} = 0.5$, $Sc_a = 10$,

$\beta_a = 0.5$, $\delta_a = 0.5$, $E_a = 0.5$, and $R_d = 2.0$. In all graphs, the outcomes were presented in the form of solid gray, blue, and red colors.

Table 3. Shear stress quantitative values for the numerous distinguished parameters.

φ	M_a	f_{wa}	Present
0.025	0.050	0.50	$2.6936103 \times 10^{-24}$
0.030	-	-	$3.0249424 \times 10^{-24}$
0.035	-	-	$3.5679915 \times 10^{-24}$
0.025	0.010	0.50	$6.1248582 \times 10^{-25}$
-	0.030	-	$2.6936103 \times 10^{-24}$
-	0.060	-	$1.4926103 \times 10^{-23}$
0.025	0.050	0.44	$2.0048851 \times 10^{-20}$
-	-	0.48	$4.2566067 \times 10^{-23}$
-	-	0.52	$5.6122940 \times 10^{-26}$
0.025	0.050	-0.05	$-2.2398001 \times 10^{-08}$
-	-	-0.10	$-1.8971081 \times 10^{-08}$
-	-	-0.15	$-1.5216356 \times 10^{-08}$

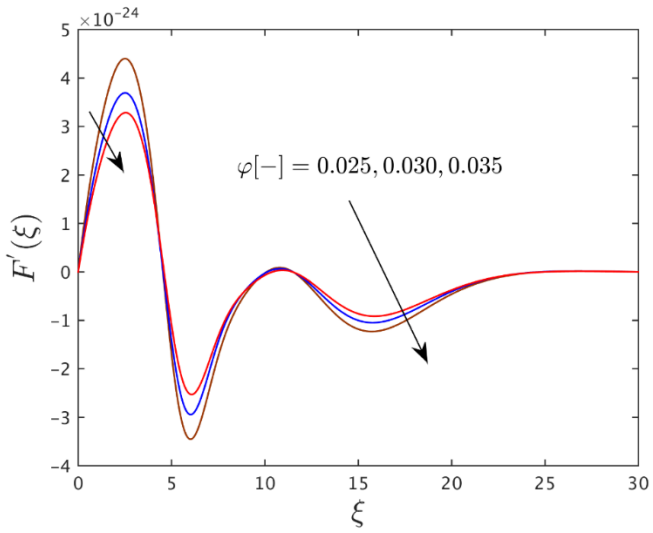

Figure 2. Velocity profile for the distinct values of φ.

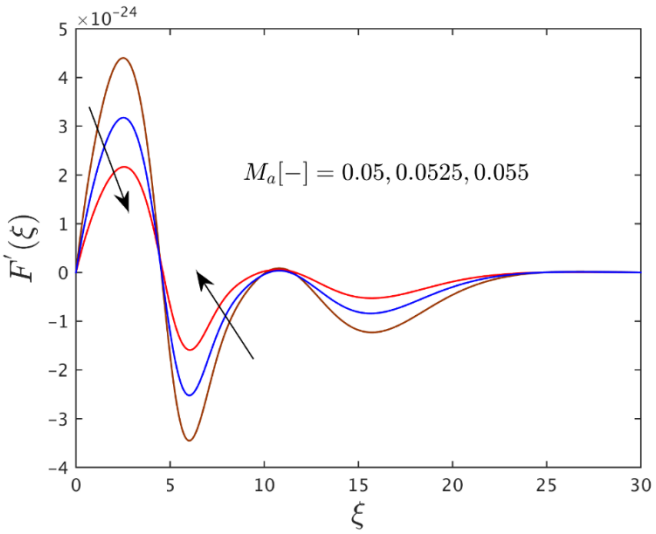

Figure 3. Velocity profile for the distinct values of M_a.

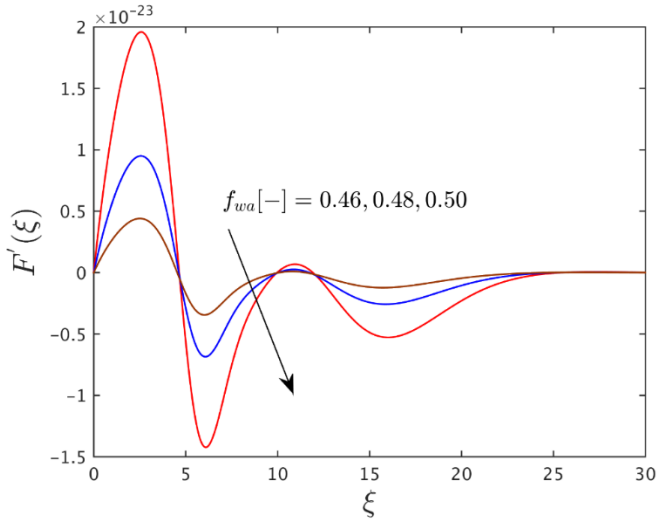

Figure 4. Velocity profile for the distinct values of f_{wa}.

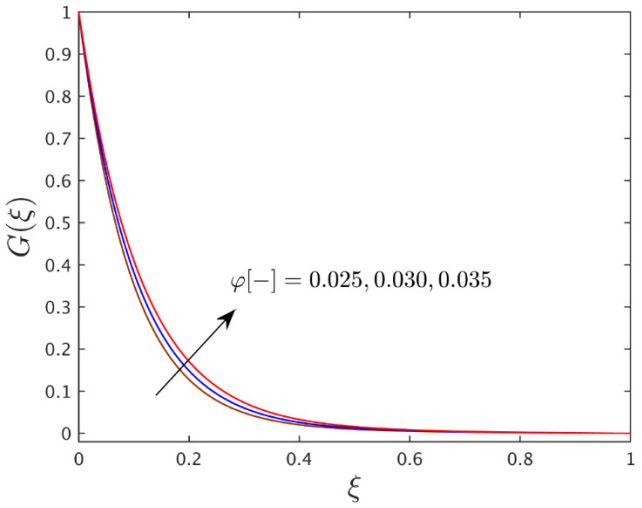

Figure 5. Temperature profile for the distinct values of φ.

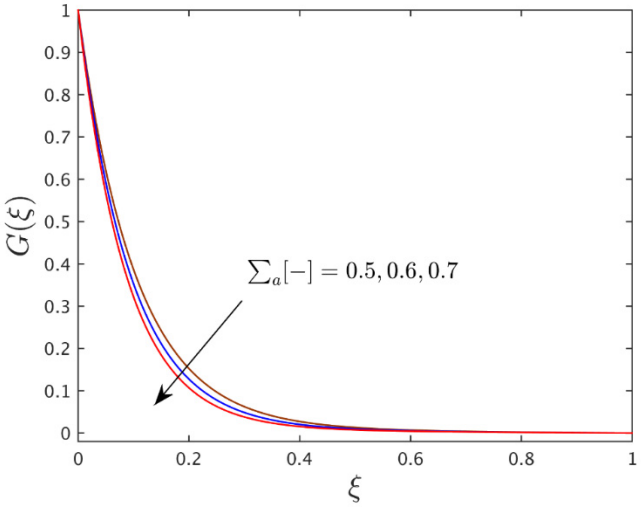

Figure 6. Temperature profile for the distinct values of Σ_a.

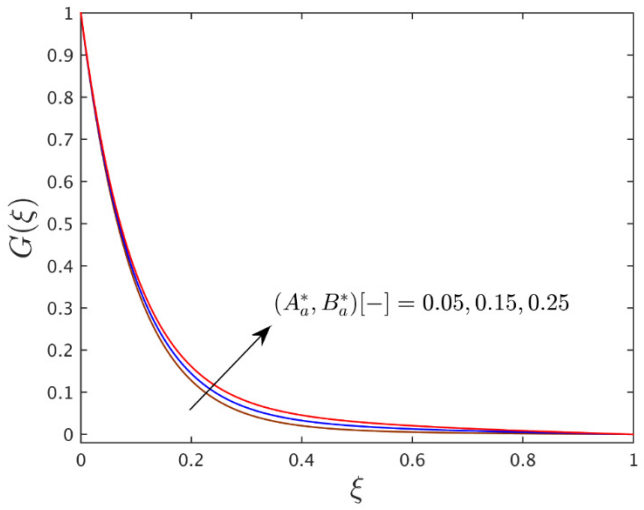

Figure 7. Temperature profile for the distinct values of $A_a^*, B_a^* > 0$.

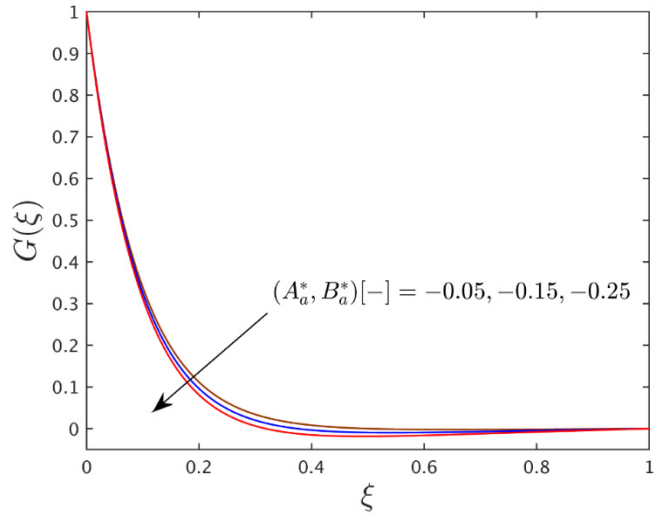

Figure 8. Temperature profile for the distinct values of $A_a^*, B_a^* < 0$.

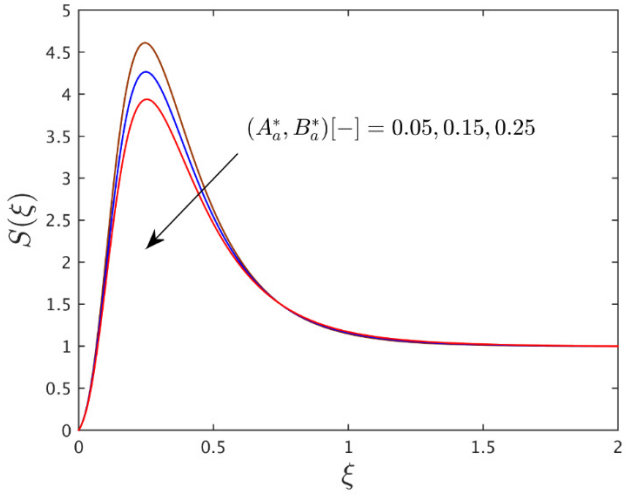

Figure 9. Concentration profile for the distinct values of $A_a^*, B_a^* > 0$.

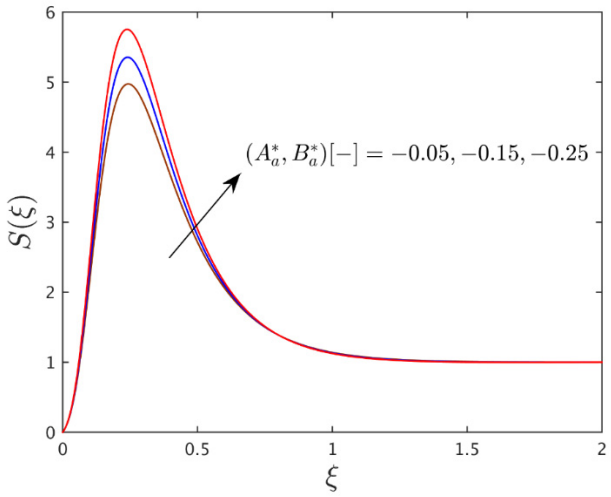

Figure 10. Concentration profile for the distinct values of $A_a^*, B_a^* < 0$.

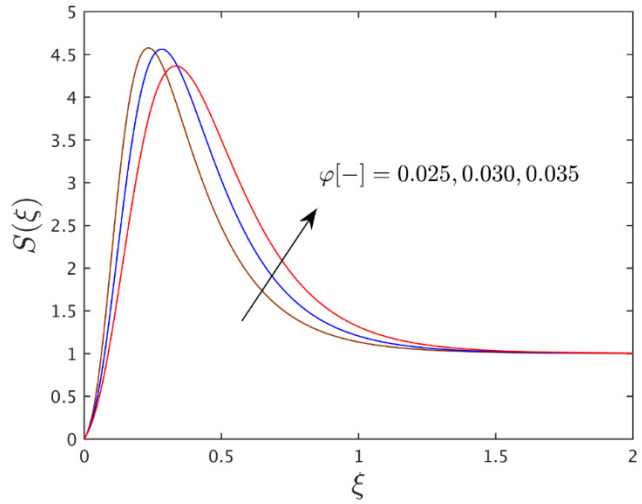

Figure 11. Concentration profile for the distinct values of φ.

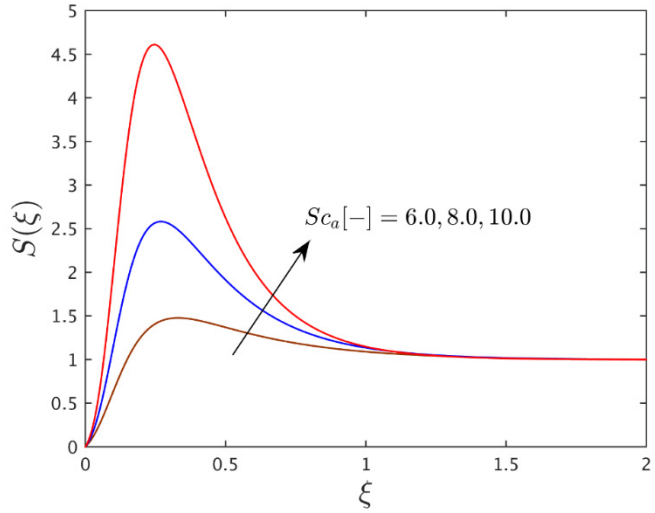

Figure 12. Concentration profile for the distinct values of Sc_a.

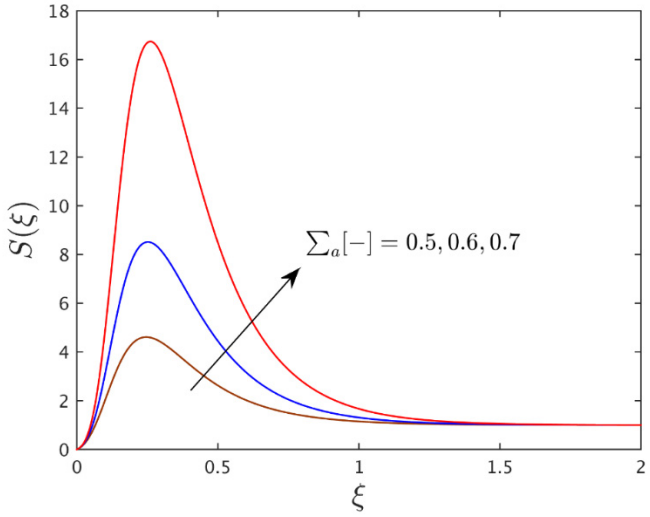

Figure 13. Concentration profile for the distinct values of Σ_a.

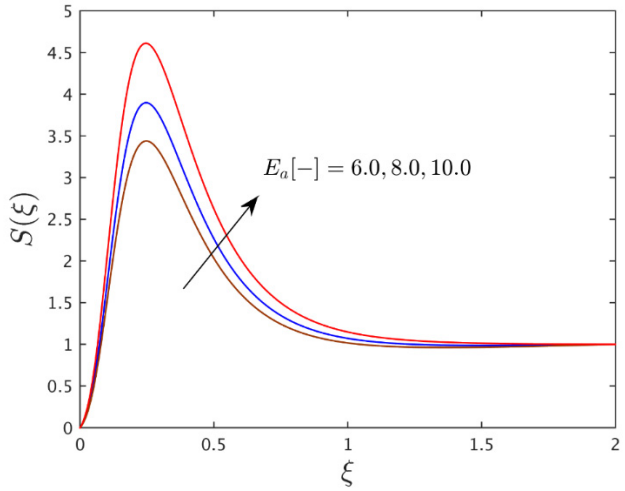

Figure 14. Concentration profile for the distinct values of E_a.

Table 4. Heat transfer quantitative values for the numerous distinguished parameters.

φ	m	f_{wa}	**Present**
0.025	1.00	0.05	11.270130
0.030	-	-	11.283560
0.035	-	-	11.297009
0.025	0.00	0.05	11.270130
-	1.00	-	11.270130
-	2.00	-	11.270130
0.025	1.00	0.10	11.150721
-	-	0.15	11.002607
-	-	0.20	10.852631
0.025	1.00	-0.10	11.725252
-	-	-0.15	11.864568
-	-	-0.20	12.002222

Table 5. Mass transfer quantitative values for the numerous distinguished parameters.

φ	Σ_a	Sc_a	δ_a	β_a	**Present**
0.025	0.50	10	0.50	0.50	4.9769350
0.030	-	-	-	-	4.9766304
0.035	-	-	-	-	4.9763215
0.025	0.50	10	0.50	0.50	4.9769350
-	0.60	-	-	-	4.9678700
-	0.70	-	-	-	4.9531125
0.025	0.50	6.00	0.50	0.50	2.9741238
-	-	8.00	-	-	3.9749540
-	-	10.0	-	-	4.9769350
0.025	0.50	10.0	0.50	0.50	4.9769350
-	-	-	1.00	-	4.9758414
-	-	-	1.50	-	4.9733595
0.025	0.50	10	0.50	0.50	4.9769350
-	-	-	-	1.00	4.9758137
-	-	-	-	1.50	4.9746928

5. Physical Interpretation of the Tables

Table 3 shows the quantitative outcome of $\left(\mu_{nf}/\mu_f\right)F''(0)$ for the single branch solutions with variations in φ, M_a, and f_{wa}. From the outcomes, it is observed that the $\left(\mu_{nf}/\mu_f\right)F''(0)$ escalates with superior values of φ,M_a, and f_{wa} while it shrinks with f_{wa}. Moreover, the magnitude of the largest and smallest shear stress values was computationally noticed due to the mass suction and injection parameter, respectively. Furthermore, the shear stress increases up to 12.3% due to the presence of nanofluid. On the other hand, the numerical values of the heat and mass transfer rates of the wall jet kerosene-oil-based graphene oxide nanoparticles were created or quantitatively constrained in Tables 4 and 5, respectively. From Table 4, it is seen that the heat-transfer rate heightens with the higher value of φ, and the generation of the heat sink parameter $A_a^*, B_a^* < 0$ but is constant throughout the domain with the precise changed value of the temperature index parameter m. Meanwhile, the impact of the heat source parameter $A_a^*, B_a^* > 0$ decreases the heat-transfer rate. Furthermore, the numerical outputs of the mass transfer rate for the various influence parameters were highlighted in Table 5**.** Here, the mass transfer rate continuously declines with the superior values of φ, β_a, δ_a, and Σ_a but augments with a higher Sc_a. In addition, the largest mass transfer rate values were observed for the values of the thermophoretic parameter. It is worth mentioning that the Nusselt number increases up to 0.119% and the Sherwood number increases up to 0.006% due to the presence of nanofluid. Whereas the Nusselt number decreases up to 1.328% in the case of suction and increases up to 1.188% due to injection. On the other hand, the Sherwood number decreases up to 0.182%, 0.021%, and 0.022% due to Σ_a, δ_a, and β_a, respectively. Whilst the Sherwood number increases up to 33.65% due to the Schmidt number.

6. Graphical Interpretation of the Velocity Profiles

Figures 2–4 exemplify the dimensionless velocity profile $F'(\xi)$ of the water-based graphene oxide nanoparticles for the solutions due to the influence of φ, M_a, and f_{wa}. Due to the cumulative effect of the influencing parameters, it is inferred from the results that the graphical behavior of the velocity profiles asymptotically converges and satisfies the boundary requirements or constraints. To explain more explicitly, the outcomes signpost in Figure 2 that the velocity field curves initially decays and then slightly improves with the growing value of φ. In other words, the wall jet velocity profile behaves distinctly versus the specific range of the pseudo-similarity variable ξ owing to the higher impressions of φ. In addition, the momentum boundary layer thickness decreases with a higher value of φ. Generally, the solid nanoparticle volume fraction improves the sign or evidence of viscosity, as a result, the motion of the wall jet flow reduces. On the other hand, the velocity

field curves initially shrink and hasten with the superior values of M_a and f_{wa} as shown in Figures 3 and 4, respectively. Later, the graphical outcomes in both profiles behave inversely in the approximate ranges of $(5 \leq \xi \leq 11)$ and $11 \leq \xi \leq 22$ with the larger values of M_a and f_{wa}. Generally, the larger impact of magnetic force creates the drag-type force called the Lorentz force. This force reaction can stop the motion of the wall jet flow, as a response, the profile of velocity decreases. Furthermore, the gap for the curves with the higher impacts of f_{wa} is slightly improved compared to the curves drawn for the value of M_a.

7. Interpretation of the Temperature Profiles

The stimulus of the solid volume fraction of nanoparticles φ and the thermophoretic particle deposition parameter Σ_a on the temperature $G(\xi)$ of the water-based graphene oxide nanomaterials flow are respectively highlighted in Figures 5 and 6. Figure 5 shows that the thermal boundary layer thickness and the temperature profile curves monotonically rise with the higher impacts of φ. Generally, the behavior was spotted due to the well-known facts. The higher impacts of a nanoparticle volume fraction creats a larger heat which significantly boosted up the values of the thermal conductivity. Therefore, the advanced thermal conductivity boosted the profile of temperature as well as the thickness of the thermal boundary layer (TTBL). Conversely, the temperature and the TTBL diminished with the superior effects of the thermophoretic parameter as shown graphically in Figure 6. Moreover, the thermophoretic parameter produces a much lower temperature because of the minimum thermal conductivity. Figures 7 and 8 demonstrate the temperature profile curves with the influence of the heat generation source and sink parameters, respectively. The outcomes reveal that temperature profile curves and the TTBL augmented with the higher impact of internal heat generation source parameter,$A_a^*, B_a^* > 0$, while it shrinks due to the generation of heat sink constraint $A_a^*, B_a^* < 0$. Physically, by adding more heat to the wall jet flow system, the heat source's presence ultimately boosts the fluid temperature. As a result, the temperature profile rises. While, in terms of physics, the heat sink factor that captivates heat from the temperature boundary layer causes the temperature profile to drop. Moreover, the TTBL rises and declines with the internal heat source and sink influences, respectively.

8. Interpretation of the Concentration Profiles

Figures 9–14 illustrate the dimensionless concentration profile $S(\xi)$ of the kerosene-oil-based graphene oxide nanoparticles flow for the branch of single outcomes with the influence of A_a^*, B_a^*, φ, Sc_a, Σ_a, and E_a. Since the relevant boundary conditions are observed to be satisfied in every graph, the behavior of the solutions asymptotically converges when the many notable parameters are varied. Figures 9 and 10 represent the influences of the erratic heat source/sink factors on the concentration profile, whereas the concentration declines with the heat source constraint but accelerates with the internal heat sink factor. Moreover, the impact of such a parameter behaves oppositely as compared to the temperature profile. The impact of φ on the concentration profile curves is shown in Figure 11, where the behavior of the profile is growing. This behavior is seen due to the higher impressions of nanoparticles because they cause a significant improvement to the kerosene-oil-based graphene nanoparticles that augment the concentration and thickness of the concentration boundary layer. Moreover, the effect of Sc_a and Σ_a on the concentration profile is depicted in Figures 12 and 13, respectively. With the superior values of Sc_a and Σ_a, the concentration and TCBL (thickness of the concentration boundary layer) enriches. This behavior is typically brought on by larger repercussions of the parameter Σ_a, which might enhance the thermophoretic coefficient k_a, and, consequently, improve the concentration profile as well as the TCBL. Finally, the E_a impact on the concentration field is graphically shown in Figure 14. Since the outcome is changed due to this term $\exp(-E_a/(1+\delta_a G))S$, it is a better tool showing how the activation energy affects the

nanoparticle concentration profile. Hence, with the larger E_a, the TCBL and profile of nanoparticle concentration upsurge.

9. Conclusions

The aim of this paper was to inspect the effect of thermophoretic particle deposition on 2D wall jet heat and mass transfer flow that carries kerosene oil-based graphene oxide nanoparticles with thermal energy and mass transpiration velocity. Further, the Arrhenius activation energy and chemical reaction along with Lorentz forces were also added to the problem. The Glauert model transformations were used to renovate the governing equations into a similarity form of ODEs, which were then numerically solved using the bvp4c method. The key findings of the current investigation are:

- With the larger value of the solid nanoparticle volume fractions, the velocity of the wall jet flow profile is moderate, while the temperature and concentration profile curves are augmented due to the higher number of nanoparticles, consequences which generate greater heat and significantly improved the thermal conductivity.
- For the advanced value of the thermophoretic parameter, the temperature profile shrinks but the profile of the concentration is boosted which might enhance the thermophoretic coefficient.
- The internal heat source factor escalates the temperature profile distribution but decelerates the concentration profiles while the influence of the internal heat sink factor is the opposite. By adding more heat to the wall jet flow system the heat source ultimately boosts the fluid temperature, whereas the heat sink factor that captivates heat from the temperature boundary layer causes the temperature profile to drop.
- Initially, the velocity profile enriches and then declines with the advanced value of the mass suction parameter.
- The shear stress progresses with the larger value of the magnetic parameter due to the Lorentz forces while it reduces magnitude-wise with the mass injection parameter.
- The solid nanoparticle volume fractions escalate the heat transfer while reducing the rate of mass transfer.
- The shear stress increases up to 12.3%, the Nusselt number increases up to 0.119%, and the Sherwood number increases up to 0.006% due to the presence of nanofluid.
- The Nusselt number decreases up to 1.328% in the case of suction and increases up to 1.188% due to injection.
- The Sherwood number decreases up to 0.182%, 0.021%, and 0.022% due to Σ_a, δ_a, and β_a, respectively.

Author Contributions: Conceptualization, U.K. and A.Z.; methodology, U.K., A.Z. and I.W.; software, U.K.; validation, Z.R., A.J., A.M.G., U.K., A.I. and I.W.; formal analysis, A.J., A.M.G. and A.I.; investigation, U.K.; resources, Z.R. and A.I.; data curation, U.K.; writing—original draft preparation, N.B., A.Z. and A.I.; writing—review and editing, Z.R., N.B., A.J., A.M.G. and A.I.; visualization, A.M.G. and U.K.; supervision, A.I.; project administration, N.B. and A.J.; funding acquisition, Z.R., A.J. and N.B. All authors have read and agreed to the published version of the manuscript.

Funding: This work was funded by the Deanship of Scientific Research at King Khalid University, Abha, Saudi Arabia, for funding this work through the Research Group Project under Grant Number (RGP.2/54/43).

Data Availability Statement: Not applicable.

Acknowledgments: The author (Z. Raizah) extends her appreciation to the Deanship of Scientific Research at King Khalid University, Abha, Saudi Arabia, for funding this work through the Research Group Project under Grant Number (RGP.2/54/43). Additionally, this research received the support from Rajamangala University of Technology Suvarnabhumi and Phuket Rajabhat University.

Conflicts of Interest: The authors declare no conflict of interest.

Nomenclature

A_a^*, B_a^*	Heat source/sink parameters
B_0	Constant magnetic field strength (Tesla)
C	Concentration
C_w	Wall concentration
C_∞	Ambient concentration
D_f	Mass diffusion coefficient
E_a	Activation energy
f_{wa}	Mass suction/injection
Q'''	Irregular heat source/sink
$k_r^2(x)$	Variable chemical reaction rate
k_a	Thermophoretic coefficient
Σ_a	Thermophoretic parameter
T_a	Reference temperature
T_w	Wall temperature (K)
T_∞	Ambient temperature (K)
T	Temperature (K)
m	Temperature index parameter
M_a	Magnetic parameter
Pr	Prandtl number
Nu_x	Nusselt number
C_f	Skin friction coefficient
Re_x	Reynolds number
Sc_a	Schmidt number
Sh_x	Sherwood number
$G(\xi)$	Dimensionless temperature
$S(\xi)$	Dimensionless concentration
k	Thermal conductivity (W/ (m·K))
V_{TPD}	Thermophoretic particle deposition
u, v	Components of velocity along the x- and y- axes (m/s)
$u_r(x)$	Reference velocity
(x, y)	Cylindrical coordinates (m)
c_p	Specific heat at constant pressure (J/ Kg·K)
Greek symbols	
β_a	Chemical reaction rate
δ_a	Temperature difference parameter
v_f	Kinematic viscosity (m^2/s)
σ	Electrical conductivity ($\Omega^{-1}m^{-1}$)
μ	Dynamic viscosity ($N{\cdot}s/m^2$)
ξ	Pseudo-similarity variable
ρ	Density (kg/m^3)
ψ	Stream function
φ	Solid nanoparticle volume fraction
Acronyms	
MHD	Magnetohydrodynamics
GO	Graphene oxide
2D	Two-dimensional
BCs	Boundary conditions
BLT	Boundary layer thickness
BLF	Boundary layer flow
NIG	Non-isothermal gas
Subscripts	
snf	Nanofluid
f	Regular base fluid
w	Wall boundary condition
∞	Far-field condition
Superscript	
$'$	Derivative with respect to ξ

References

1. Balazs, A.C.; Emrick, T.; Russell, T.P. Nanoparticle Polymer Composites: Where Two Small Worlds Meet. *Science* **2006**, *314*, 1107–1110. [CrossRef] [PubMed]
2. Yu, C.; Kim, Y.S.; Kim, D.; Grunlan, J.C. Thermoelectric Behavior of Segregated-Network Polymer Nanocomposites. *Nano Lett.* **2008**, *8*, 4428–4432. [CrossRef] [PubMed]
3. Bakunin, V.; Suslov, A.; Kuzmina, G.; Parenago, O.; Topchiev, A. Synthesis and Application of Inorganic Nanoparticles as Lubricant Components—A Review. *J. Nanopart. Res.* **2004**, *6*, 273–284. [CrossRef]
4. Li, W.; Zheng, S.H.; Cao, B.Q.; Ma, S. Friction and wear properties of ZrO_2/SiO_2 composite nanoparticles. *J. Nanopart. Res.* **2010**, *13*, 2129–2137. [CrossRef]
5. Wu, Z.-S.; Ren, W.; Wen, L.; Gao, L.; Zhao, J.; Chen, Z.; Zhou, G.; Li, F.; Cheng, H.-M. Graphene Anchored with Co_3O_4 Nanoparticles as Anode of Lithium Ion Batteries with Enhanced Reversible Capacity and Cyclic Performance. *ACS Nano* **2010**, *4*, 3187–3194. [CrossRef]
6. Pumera, M. Graphene-based nanomaterials for energy storage. *Energy Environ. Sci.* **2010**, *4*, 668–674. [CrossRef]
7. Ahmad, I.; McCarthy, J.E.; Baranoy, A.; Gun'ko, Y.K. Development of graphene nanoplate based counter electrodes for solar cells. *Materials* **2015**, *8*, 5953–5973. [CrossRef]
8. Khan, N.S.; Gul, T.; Islam, S.; Khan, I.; Alqahtani, A.M.; Alshomrani, A.S. Magnetohydrodynamic Nanoliquid Thin Film Sprayed on a Stretching Cylinder with Heat Transfer. *J. Appl. Sci.* **2017**, *7*, 271. [CrossRef]
9. Zuhra, S.; Khan, N.S.; Khan, M.A.; Islam, S.; Khan, W.; Bonyah, E. Flow and heat transfer in water based liquid film fluids dispensed with graphene nanoparticles. *Results Phys.* **2018**, *8*, 1143–1157. [CrossRef]
10. Khan, U.; Zaib, A.; Ishak, A.; Waini, I.; Pop, I. Mixed Convection Flow of Water Conveying Graphene Oxide Nanoparticles over a Vertical Plate Experiencing the Impacts of Thermal Radiation. *Mathematics* **2022**, *10*, 2833. [CrossRef]
11. Alam, M.; Rahman, M.; Sattar, M. Effects of variable suction and thermophoresis on steady MHD combined free-forced convective heat and mass transfer flow over a semi-infinite permeable inclined plate in the presence of thermal radiation. *Int. J. Therm. Sci.* **2008**, *47*, 758–765. [CrossRef]
12. Damseh, R.A.; Tahat, M.S.; Benim, D.-I.H.A.C. Nonsimilar solutions of magnetohydrodynamic and thermophoresis particle deposition on mixed convection problem in porous media along a vertical surface with variable wall temperature. *Prog. Comput. Fluid Dyn. Int. J.* **2009**, *9*, 58. [CrossRef]
13. Rahman, M.M. Thermophoretic deposition of nanoparticles due to a permeable rotating disk: Effects of partial slip, magnetic field, thermal radiation, thermal diffusion, and diffusion thermo. *Int. J. Math. Comput. Phys. Electr. Comput. Eng.* **2013**, *7*, 899–911.
14. Doh, D.-H.; Muthtamilselvan, M.; Swathene, B.; Ramya, E. Homogeneous and heterogeneous reactions in a nanofluid flow due to a rotating disk of variable thickness using HAM. *Math. Comput. Simul.* **2020**, *168*, 90–110. [CrossRef]
15. Gowda, R.P.; Kumar, R.N.; Aldalbahi, A.; Issakhov, A.; Prasannakumara, B.; Rahimi-Gorji, M.; Rahaman, M. Thermophoretic particle deposition in time-dependent flow of hybrid nanofluid over rotating and vertically upward/ downward moving disk. *Surf. Interfaces* **2021**, *22*, 100864. [CrossRef]
16. Waini, I.; Khan, U.; Zaib, A.; Ishak, A.; Pop, I. Thermophoresis particle deposition of $CoFe_2O_4$-TiO_2 hybrid nanoparticles on micropolar flow through a moving flat plate with viscous dissipation effects. *Int. J. Numer. Methods Heat Fluid Flow* **2022**, *32*, 3259–3282. [CrossRef]
17. Bashir, M.N.; Rauf, A.; Shehzad, S.A.; Ali, M.; Mushtaq, T. Thermophoresis phenomenon in radiative flow about vertical movement of a rotating disk in porous region. *Adv. Mech. Eng.* **2022**, *14*, 16878132221115019. [CrossRef]
18. Bashir, S.; Ramzan, M.; Ghazwani, H.A.S.; Nisar, K.S.; Saleel, C.A.; Abdelrahman, A. Magnetic Dipole and Thermophoretic Particle Deposition Impact on Bioconvective Oldroyd-B Fluid Flow over a Stretching Surface with Cattaneo–Christov Heat Flux. *Nanomaterials* **2022**, *12*, 2181. [CrossRef]
19. Shafique, Z.; Mustafa, M.; Mushtaq, A. Boundary layer flow of Maxwell fluid in rotating frame with binary chemical reaction and activation energy. *Results Phys.* **2016**, *6*, 627–633. [CrossRef]
20. Khan, W.A.; Sultan, F.; Ali, M.; Shahzad, M.; Khan, M.; Irfan, M. Consequences of activation energy and binary chemical reaction for 3D flow of Cross-nanofluid with radiative heat transfer. *J. Braz. Soc. Mech. Sci. Eng.* **2019**, *41*, 4. [CrossRef]
21. Khan, M.I.; Alzahrani, F. Binary chemical reaction with activation energy in dissipative flow of non-Newtonian nanomaterial. *J. Theor. Comput. Chem.* **2020**, *19*, 2040006. [CrossRef]
22. Najafabadi, M.F.; Rostami, H.T.; Hosseinzadeh, K.; Ganji, D.D. Thermal analysis of a moving fin using the radial basis function approximation. *Heat Transf.* **2021**, *50*, 7553–7567. [CrossRef]
23. Rana, B.; Arifuzzaman, S.; Islam, S.; Reza-E-Rabbi, S.; Al-Mamun, A.; Mazumder, M.; Roy, K.C.; Khan, S. Swimming of microbes in blood flow of nano-bioconvective Williamson fluid. *Therm. Sci. Eng. Prog.* **2021**, *25*, 101018. [CrossRef]
24. Reza-E-Rabbi, S.; Ahmmed, S.F.; Islam, S.; Arifuzzaman, S.M.; Rana, B.M.J.; Ali, Y.; Al-Mamun, A.; Khan, S. Characterization of fluid flow and heat transfer of a periodic magnetohydrodynamics nano non-Newtonian liquid with Arrhenius activation energy and nonlinear radiation. *Heat Transf.* **2022**. [CrossRef]
25. Goren, S.L. Thermophoresis of aerosol particles in the laminar boundary layer on a flat plate. *J. Colloid Interface Sci.* **1977**, *61*, 77–85. [CrossRef]
26. Talbot, L.; Cheng, R.K.; Schefer, R.W.; Willis, D.R. Thermophoresis of particles in a heated boundary layer. *J. Fluid Mech.* **1980**, *101*, 737–758. [CrossRef]

27. Mills, A.; Xu, H.; Ayazi, F. The effect of wall suction and thermophoresis on aerosol particle deposition from a laminar boundary layer on a flat plate. *Int. J. Heat Mass Transf.* **1984**, *27*, 1110–1113. [CrossRef]
28. Batchelor, G.; Shen, C. Thermophoretic deposition of particles in gas flowing over cold surfaces. *J. Colloid Interface Sci.* **1985**, *107*, 21–37. [CrossRef]
29. Tsai, R. A simple approach for evaluating the effect of wall suction and thermophoresis on aerosol particle deposition from a laminar flow over a flat plate. *Int. Commun. Heat Mass Transf.* **1999**, *26*, 249–257. [CrossRef]
30. Chamkha, A.J.; Issa, C. Effects of heat generation/absorption and thermophoresis on hydromagnetic flow with heat and mass transfer over a flat surface. *Int. J. Numer. Methods Heat Fluid Flow* **2000**, *10*, 432–449. [CrossRef]
31. Chamkha, A.J.; Pop, I. Effect of thermophoresis particle deposition in free convection boundary layer from a vertical flat plate embedded in a porous medium. *Int. Commun. Heat Mass Transf.* **2004**, *31*, 421–430. [CrossRef]
32. Alam, M.; Rahman, M.; Sattar, M. On the effectiveness of viscous dissipation and Joule heating on steady Magnetohydrodynamic heat and mass transfer flow over an inclined radiate isothermal permeable surface in the presence of thermophoresis. *Commun. Nonlinear Sci. Numer. Simul.* **2009**, *14*, 2132–2143. [CrossRef]
33. Das, K.; Jana, S.; Kundu, P. Thermophoretic MHD slip flow over a permeable surface with variable fluid properties. *Alex. Eng. J.* **2015**, *54*, 35–44. [CrossRef]
34. Sinha, A.; Misra, J.C. Mixed Convection Hydromagnetic Flow with Heat Generation, Thermophoresis and Mass Transfer over an Inclined Nonlinear Porous Shrinking Sheet: A Numerical Approach. *J. Mech.* **2014**, *30*, 491–503. [CrossRef]
35. Zaib, A.; Shafie, S. Slip Effect on an Unsteady MHD Stagnation-Point Flow of a Micropolar Fluid towards a Shrinking Sheet with Thermophoresis Effect. *Int. J. Comput. Methods Eng. Sci. Mech.* **2015**, *16*, 285–291. [CrossRef]
36. Jyothi, A.M.; Kumar, R.S.V.; Madhukesh, J.K.; Prasannakumara, B.C.; Ramesh, G.K. Squeezing flow of Casson hybrid nanofluid between parallel plates with a heat source or sink and thermophoretic particle deposition. *Heat Transf.* **2021**, *50*, 7139–7156. [CrossRef]
37. Shah, N.A.; Yook, S.-J.; Tosin, O. Analytic simulation of thermophoretic second grade fluid flow past a vertical surface with variable fluid characteristics and convective heating. *Sci. Rep.* **2022**, *12*, 5445. [CrossRef] [PubMed]
38. Tetervin, N. *Laminar Flow of a Slightly Viscous Incompressible Fluid that Issues from a Slit and Passes over a Flat Plate*; No. 1644; NACA TN: Washington, DC, USA, 1948; p. 40.
39. Glauert, M.B. The wall jet. *J. Fluid Mech.* **1965**, *1*, 625–643. [CrossRef]
40. Riley, N. Effects of compressibility on a laminar wall jet. *J. Fluid Mech.* **1958**, *4*, 615–628. [CrossRef]
41. Schwarz, W.H.; Caswell, B. Some heat transfer characteristics of the two-dimensional laminar incompressible wall jet. *Chem. Eng. Sci.* **1961**, *16*, 338–351. [CrossRef]
42. Gorla, R.S.R. Unsteady heat transfer characteristics of a two dimensional laminar wall jet. *Int. J. Eng. Sci.* **1973**, *11*, 841–851. [CrossRef]
43. Aly, E.H.; Pop, I. Merkin and Needham wall jet problem for hybrid nanofluids with thermal energy. *Eur. J. Mech.—B Fluids* **2020**, *83*, 195–204. [CrossRef]
44. Chiam, T.C. Hydromagnetic flow over a surface with a power law velocity. *Int. J. Eng. Sci.* **1995**, *33*, 429–435. [CrossRef]
45. Sheikholeslami, M.; Gorji-Bandpay, M.; Ganji, D.D.G.-D. Magnetic field effects on natural convection around a horizontal circular cylinder inside a square enclosure filled with nanofluid. *Int. Commun. Heat Mass Transf.* **2012**, *39*, 978–986. [CrossRef]
46. Khan, U.; Zaib, A.; Ishak, A.; Sherif, E.-S.M.; Waini, I.; Chu, Y.-M.; Pop, I. Radiative mixed convective flow induced by hybrid nanofluid over a porous vertical cylinder in a porous media with irregular heat sink/source. *Case Stud. Therm. Eng.* **2022**, *30*, 101711. [CrossRef]
47. Raees, A.; Xu, H.; Raees-Ul-Haq, M. Explicit solutions of wall jet flow subject to a convective boundary condition. *Bound. Value Probl.* **2014**, *2014*, 163. [CrossRef]
48. Hossain, R.; Azad, A.; Hasan, J.; Rahman, M. Thermophysical properties of Kerosene oil-based CNT nanofluid on unsteady mixed convection with MHD and radiative heat flux. *Eng. Sci. Technol. Int. J.* **2022**, *35*, 101095. [CrossRef]
49. Waini, I.; Ishak, A.; Pop, I. MHD Glauert Flow of a Hybrid Nanofluid with Heat Transfer. *J. Adv. Res. Fluid Mech. Therm. Sci.* **2021**, *86*, 91–100. [CrossRef]